Journal of Environmental and Engineering Geophysics

December 2023
Volume 28
Issue 4
pp. 155–168
DOI: #10.32389/JEEG23-002

Characterization of a Small Abandoned Municipal Solid Waste Scattered Landfill Combining Remote Sensing and Near-Surface Geophysical Investigations

Grégory Bièvre[1,*] and Stéphane Garambois[1]

[1]Univ. Grenoble Alpes, Univ. Savoie Mont Blanc, CNRS, IRD, Univ. Gustave Eiffel, ISTerre, Grenoble, 38000, France

*Corresponding author: gregory.bievre@univ-grenoble-alpes.fr

ABSTRACT

This study reports the combination of remote sensing and ground geophysical techniques to locate an abandoned and hidden municipal solid waste landfill located in a fluvial plain in the French Western Alps. Following earthworks and further floods that eroded into the river bank, wastes made of a mixture of plastic, metal and soil/earth, were uncovered and some of them flowed into the river. The existence of an abandoned landfill, several decades-old, was known, but the knowledge of its exact location was forgotten. Historic aerial photographs back to 1948 allowed delineation in space and time of the location of a platform that was used for landfill operations between around 1973 and 1983. A LiDAR DEM acquired in 2012 allowed was used to locate topographic depressions 0.1 to 0.4 m in depth, notably inside the platform. These depressions are interpreted as resulting from differential compaction originating from the presence of compressible wastes. Geophysical mapping techniques (magnetic and electromagnetic) confirmed the presence of anomalies inside the identified platform. Geophysical imaging techniques (ground-penetrating radar, electrical resistivity tomography) provided a quantitative evaluation of the width and depth of the individual pits. The combination of the different techniques allowed for estimating the first-order volume of waste. The methodology adopted in this work is applicable to detect landfills exhibiting differential compaction and physical contrasts.

INTRODUCTION

During the past 50 years, municipal solid waste (MSW) landfills evolved worldwide from uncontrolled dumping to sanitary landfills townsend2015. Consequently, numerous old MSW landfills, often several decades old, were abandoned and many of them are now hidden or forgotten (Biotto *et al.*, 2009; Soupios & Ntarlagiannis, 2017), not to mention illegal landfills. This is especially the case for small municipalities with reduced to non-existing technical departments. These abandoned or illegal landfills generally have poor to no protection and represent potential environmental threats. As such, their detection remains a challenging but crucial task.

Classic geotechnical prospecting (*e.g.* boreholes, penetrometer tests) is a straightforward approach to detecting such structures. However, in the case landfills are made of individual pits with reduced spatial extents (each a few m wide), these punctual measurements need to be conducted with high spatial density to be efficient. An alternative, more cost-effective approach is to perform non-invasive and spatially integrative prospecting such as remote sensing and geophysics. Remote sensing has been used to detect and characterize landfill evolution using diachronic aerial optical (Di Fiore *et al.*, 2017) or multi-spectral images (Silvestri & Omri, 2008). Aerial photographs can also be combined with high-resolution surface morphology, *e.g.* provided by the Light Detection And Ranging (LiDAR) technique, to precisely delineate the extent of abandoned landfills (De Wet, 2016). Another potential remote sensing technique is Interferometric Synthetic Aperture Radar (InSAR). This technique provides high vertical accuracy (of the order of the cm). However, the spatial resolution is of a few m and this approach is more adapted to structures several km^2 in surface (Baek *et al.*, 2019). Furthermore, since there needs a difference in elevation to detect landfills, a multi-temporal approach is required during which the surveyed structures must endure subsidence.

Ground geophysical techniques have long been applied to landfill investigation. Notably, Green *et al.* (1999) proposed a template for the investigation of small landfills using various geophysical parameters (seismic, magnetic, electromagnetic). Since then, numerous papers reported the successful integration of geophysical methods to delineate and characterize landfills (Soupios *et al.*, 2007; Dumont *et al.*, 2017; Appiah *et al.*, 2018; Di Maio *et al.*, 2018; Osinowo *et al.*, 2018; Yannah *et al.*, 2019; Kondracka *et al.*, 2021). They all proposed a similar approach, consisting of using first mapping techniques (magnetics,

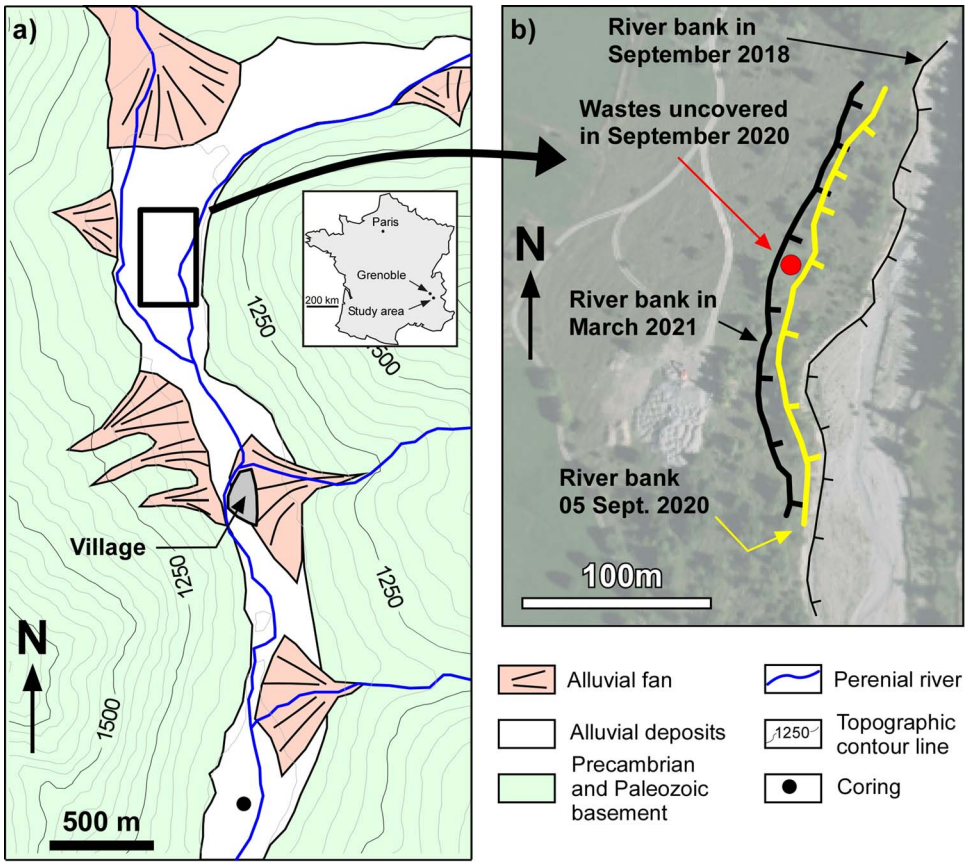

Figure 1 Location and geological setting of the study site. **a)** Geological map simplified from the French Geological Survey (BRGM; infoterre.brgm.fr). Slope deposits are not represented. The black rectangle highlights the study site. **b)** Orthophotography of September 2018 showing the location of the western river bank at that time, on 05 September 2020 (from Google satellite) and in March 2021.

electromagnetics) and, second, more punctual techniques providing quantitative information with depth such as electrical resistivity tomography (ERT) or ground-penetrating radar (GPR).

The combination of remote sensing and ground geophysics was reported only recently for landfill investigation. Martínez-Segura *et al.* (2020) combined LiDAR and ERT to evaluate the volume of known landfills. To our knowledge, the combination of remote sensing and geophysical techniques to specifically detect abandoned or forgotten landfills has never been reported. This paper aims to report the successful detection of a small, abandoned MSW landfill made of several individual pits a few m wide. The precise location of the pits was forgotten but two successive floods uncovered wastes in mid-February 2019 and September 2020. In this context, the key point for stakeholders is to locate precisely the MSW and delineate its spatial extent. Notably, did the uncovered wastes correspond to an isolated and punctual pit or the main historical landfill area? If yes, further floods and subsequent bank erosion may uncover other MSW pits and wash the wastes downstream. The determination of the spatial extent of the MSW landfill and each pit in the landfill is then required to design and evaluate the cost of the further required works to either uncover, sort and manage, or isolate and protect this historical landfill. The methodology developed in this work can be applied to any landfill exhibiting undergoing or past subsidence associated with physical contrasts between the waste material and the soil.

STUDY SITE

The study site is a mountain valley located in the French western Alps, a few tens of km South-East of Grenoble (Fig. 1a). For confidentiality reasons, however, the exact location is not be provided. The geological substratum is made of Precambrian and Paleozoic, dominantly metamorphic, impervious rocks. The valley is filled with Quaternary fluvial loose sediments. Very few geological data are available from the study site. The closest geological data originates from coring conducted in late 1999, 3 km south of the study site (Fig. 1a), the data of which were retrieved from the French Geological Survey (BRGM; infoterre.brgm.fr). The lithological log of this 40.5 m-deep coring reveals the continuous presence of a mixture of grains ranging from sand to cobble with, however, the occurrence of finer deposits (silts and fine sands) between 5.5 and 8.6 m depth. Water was observed at around 9-10 m depth at the end of the drilling operation but no piezometer data are available.

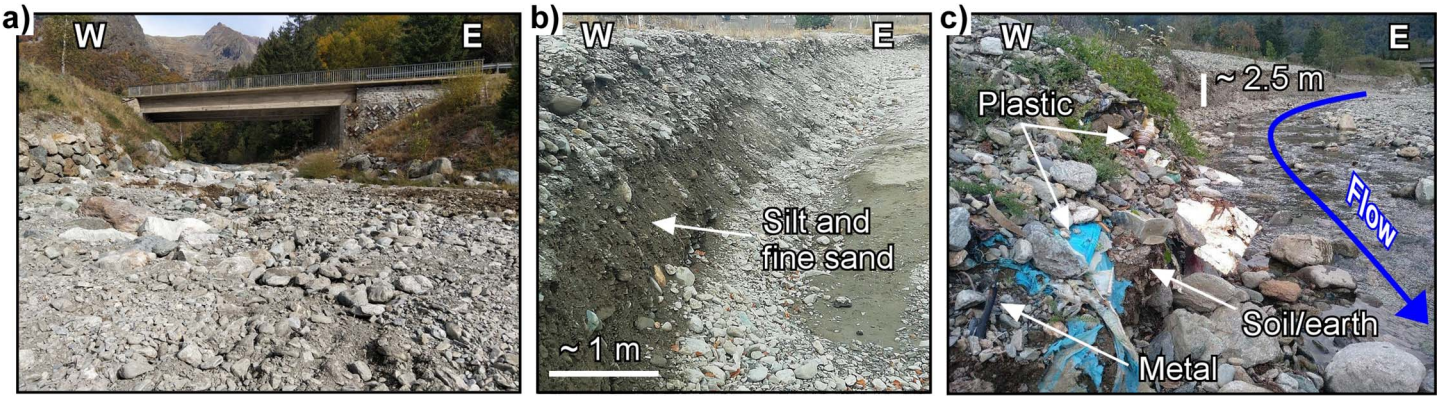

Figure 2 Lithological and waste facies. **a)** Coarse sand to cobbles. **b)** Silt and fine sand. **c)** Uncovered landfill following the flood of September 2020.

These observations suggest that, in the alluvial plain, the first tens of metres correspond to loose, permeable sediments which contain a groundwater table.

Following a flood and a massive transport of sediments that threatened a village located 1 km south of the study site (Fig. 1a) in 2008, hydraulic and geotechnical studies were conducted in the early 2010s to understand and mitigate this risk. They notably showed that, on the study site, the width of the floodplain was reduced by two between 1950 and 2010, thus preventing sedimentation in this area as was the case before. Following these studies, earthworks were designed and further conducted in late 2018 to enlarge the floodplain. The first objective was to reduce the flow strength and sediment transportation downstream, but also to allow lateral movements of the river bed. The second objective was to restore the morphological conditions necessary for proper ecological functioning. This resulted in the cut and westward displacement of up to 40 m of the western bank of the river (Fig. 1b). At the time works were designed, the existence of the historic MSW landfill was known but the knowledge of its exact location was forgotten. It was assumed to be further west than its actual location and made of several individual pits with maximum widths and depths of a few m. Although these earthworks did not detect any MSW landfill, two floods occurred in mid-February 2019 and in September 2020 and eroded into the western bank. First, this erosion allows direct observations on the study site, namely along the eroded river bank. It shows the predominance of horizons mainly made of coarse sand to cobbles (Fig. 2a). However, layers containing finer deposits (silt to sand), several tens of centimetres thick, are also observed in places (Fig. 2b). Second, the last flood uncovered wastes (Fig. 2c). These MSWs are mainly composed of a mixture of plastic, metal and soil/earth. After sorting operations, the ratio of waste/soil was evaluated to around 2 in weight.

Emergency mitigation works were conducted in October 2021. They mainly consisted of the setting of rock rip-rap along the western bank to protect it from further potential floods which could lead to the uncovering and transport of MSW into the river bed and the floodplain. Finally, 10 excavations were conducted in October 2022 to depths of 3 m. They were localized over some pits identified by geophysical investigation.

MATERIALS AND METHODS

Remote Sensing

Ten aerial photographs from 1948 to 1993 were retrieved from the French National Geographic Institute (IGN; remonterletemps.ign.fr). They were orthorectified manually, using around 15 ground control points originating from a georeferenced Landsat/Copernicus image from 05 September 2020 and retrieved from Google Satellite services. Five orthorectified aerial photographs from 1998 to 2018 were also used (source French National Geographic Institute; IGN). These 16 images were used to identify the period during which landfill works were conducted over the study site and the perimeters of earthworks were manually digitized.

An airborne LiDAR laser scanner was acquired in 2012. The resulting Digital Elevation Model (DEM) presents a spatial resolution of 1 m and vertical accuracy of the order of the cm. Data were analysed in terms of surface morphology where remarkable features were manually digitized. Slope analysis was also conducted but did not provide supplementary observation. It will not be presented.

Geophysical Methods

All the geophysical techniques used in this work are classical and are detailed in reference books (*e.g.* Keary *et al.*, 2002; Reynolds, 2011) that are used to describe them briefly hereafter. Geophysical measurements were acquired in March 2021 (magnetics, electromagnetics, Ground-Penetrating Radar) with a snow height of around 0.2 m, and in May and June 2021 (seismics, Electrical Resistivity Tomography). Locations of the different measurements are shown in Fig. 3.

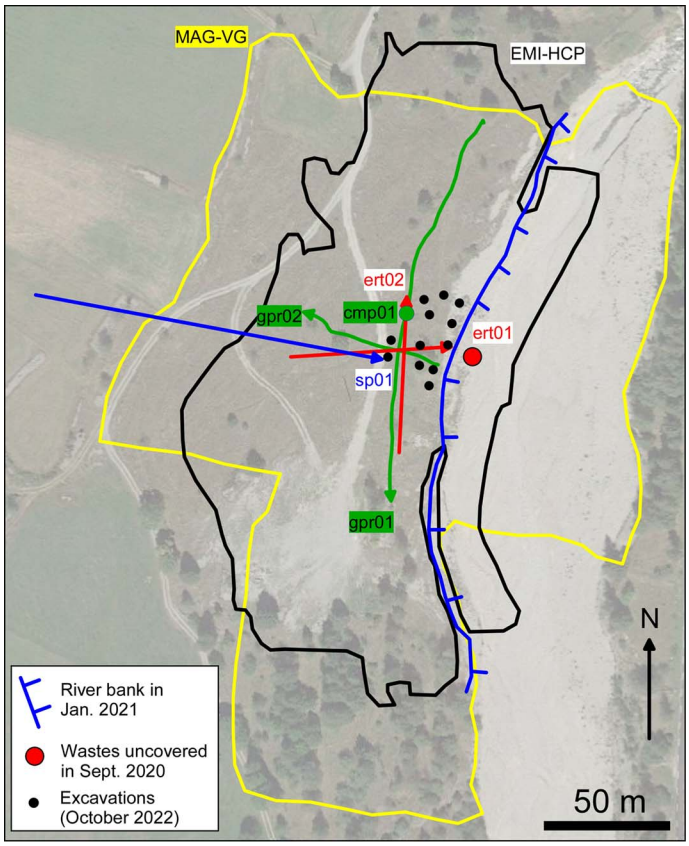

Figure 3 Locations of geophysical measurements. The satellite image dates from 05 September 2020. MAG-VG: vertical gradient of the magnetic field; EMI-HCP: electromagnetic induction in horizontal coplanar mode; sp01: seismic profile; gpr01 and gpr02: ground-penetrating radar profiles; cmp01: common mid-point GPR profile; ert01 and ert02: electrical resistivity tomography. The red dot corresponds to the uncovered wastes shown in Figure 2c.

Magnetic mapping. Magnetic prospecting is based on the measure of the Earth's magnetic field (B, generally expressed in nT). Most natural minerals have a weak to null magnetic susceptibility, except magnetite and a few other ferruginous minerals. The method is then suited to detect anthropogenic deposits and artefacts such as wastes and archaeological remains. Measurements were conducted using a GSM-19 GW Overhauser magnetometer (GEM Systems, Inc., Ontario, Canada), which does not present instrumental drift, according to the manufacturer. The device provides an accuracy of the order of ± 0.1 nT and a resolution of 0.01 nT. The device is carried by the operator and measurements were acquired in a random walking mode (i.e. no specific profile nor orientation were defined) with a sampling periodicity of 0.5 s. It was only chosen to concentrate more measurements over the perimeter of earthworks identified from the remote sensing analysis. Measurements were directly georeferenced using a Global Navigation Satellite System (GNSS) coupled to the magnetometer. The accuracy of the positioning with such a device is of the order of the metre when the site is unobstructed. A first sensor provides the measure of the total intensity of the magnetic field (expressed in nT). A second sensor, located vertically 0.56 m above the first one, allows for the calculation of the local vertical gradient (expressed in nT/m) by subtracting the two measures. This approach allows for getting rid of potential temporal variations and focusing on local anomalies. This approach was used in this work. Experimental data were filtered from noisy data, notably originating from identified anomalies (*e.g.* metallic fences). They were then interpolated using a grid spacing of the order of 1 m^2 to produce a map depicting the spatial variability of the vertical gradient of the magnetic field.

Electromagnetic induction mapping. Electromagnetic Induction (EMI) mapping was conducted using an EM 31 conductivity meter (Geonics Ltd, Ontario, Canada). A transmitting coil Tx generates a primary EM field (H_p) at a frequency of 9.8 kHz. The presence of conductive bodies in the ground leads to the creation of eddy currents which generate a secondary EM fields (H_s). A receiver coil Rx (distance Tx-Rx of around 3.6 m with this device) detects the resulting air primary and secondary fields, which will differ in both phase and amplitude. The ratio between H_s and H_p is directly proportional to the apparent electrical conductivity (σ_a, in S/m) or its inverse, the apparent electrical resistivity (ρ_a, in Ωm).

The device is carried by the operator and measurements were acquired with a sampling period of 1 s, using the same random walking mode approach than for magnetic mapping. Measures were directly georeferenced using a GNSS coupled to the conductivity meter and providing an accuracy of the order of the metre when the site is unobstructed. Measurements are possible with 2 coil mode orientation: Horizontal Co-Planar (HCP) and Vertical Co-Planar (VCP) coil orientation modes. Since results are redundant with the 2 modes, it is chosen to expose measurements obtained using the HCP mode only, because of the hypothesis that the base of the pits could reach a maximum depth of 4 m. In the HCP configuration, the EM field is vertical (perpendicular to the plane defined by the coils) and measurements are sensitive down to a depth of around 5-6 m. The measured apparent resistivity is then an integrated value of the ground apparent resistivity between the surface and this depth (McNeill, 1980).

Data processing mainly consists of filtering noisy data (*e.g.* metallic elements observed at the surface). Data were then interpolated to build a map depicting the spatial variability of apparent resistivity (grid size of the order of 1 m^2). The device also provides the measure of the magnetic susceptibility (the "in-phase" ratio of the secondary to the primary magnetic field). Unfortunately, technical issues during the campaign did not allow for measuring this parameter.

Seismics. A seismic profile was conducted using two Geode seismometers (Geometrics, CA, USA) connected to 48 vertical geophones (nominal frequency of 4.5 Hz) regularly spread each 3 m along a straight line. Two end-shots and three in-shots were used to perform refraction and tomographic analyses. Seismic sources consisted of a stack of sledgehammer (5 kg) shots vertically hitting a plate. Seismograms were recorded during 2 s with a sampling frequency of 2000 Hz. The location of each geophone and source was measured using a Real-Time Kinematics (RTK) differential GNSS providing an accuracy of the order of a few cm. First arrivals were manually picked and initially analyzed only considering the two extreme shots for a refraction approach, using the Sardine software (Demanet, 2000). 179 traveltimes were then inverted using a tomography approach through the pyGIMLi package (Rücker *et al.*, 2017). From a statistical point of view, the inversion performed using the L2 norm converged satisfactorily after a few iterations to $\chi^2 \approx 1$ and a relative root-mean-square error (RRMSE) below 5%. The χ^2 stopping criteria (Friedel, 2003; Günther *et al.*, 2006) reads:

$$\chi^2 = \frac{1}{n}\sum_{i=1}^{n}\left(\frac{d_i - m_i}{e_i}\right)^2 \quad (1)$$

where n is the number of measurements, i is the rank of the measurement, d_i and m_i are the experimental and theoretical data of rank i, respectively, and e_i is an experimental error. This last encompasses a systematic error (default value of 3%), an error on the picked traveltime estimated to 0.5 ms (and on the measured electrical resistance in the case of electrical resistivity tomography; see next section) and, finally, an error related to the location of the sensors (0.05 m in this work).

Electrical resistivity tomography. Electrical resistivity tomography (ERT) provides images of the underground distribution of electrical resistivity, which characterises the ability of a medium to oppose the flow of electrical current. The technique consists in injecting electric current through two electrodes and measuring the voltage induced using two other electrodes. These measurements provide the distribution of apparent resistivity ρ_a (Ωm) along the profile and as a function of a pseudo-depth which is related to the spacing of the measuring electrodes. The resistivity (ρ, in Ωm) distribution along the profile and as a function of depth is obtained by inversion of apparent resistivity. Measurements were conducted with a Terrameter LS multi-channel resistivity meter (Guideline Geo AB, Sweden) for two profiles using 63 (profile ert01) and 64 (profile ert02) stainless steel electrodes regularly spread each 1 m along a straight line. The profiles are oriented north-south (ert01) and west-east (ert02), and they are localized in Fig. 3. The location of each electrode was measured using an RTK differential GNSS. Resistivity measurements were acquired using a multi-gradient configuration (Dahlin & Zhou, 2006) which provided 1 279 and 1 390 experimental data for ert01 and ert02, respectively. Apparent resistivity data were inverted using the Boundless Electrical Resistivity Tomography algorithm (Günther *et al.*, 2006), including topography (Rücker *et al.*, 2006). Data were inverted using the L1 norm. From a statistical point of view, each inversion converged satisfactorily after a few iterations to $\chi^2 \approx 1$ and mean absolute errors below 5%.

Ground-Penetrating radar. Ground-Penetrating Radar (GPR) measurements consist of the analysis of the reflectivity of an electromagnetic (EM) signal emitted from a transmitting to a receiving antenna (the two antennas are close to each other) both in contact with the ground. The reflectivity of the medium, which depends on the contrasts in the dielectric, magnetic or electrical properties between two layers, allows imaging of the lateral continuity of interfaces separating two layers or detecting small objects through the presence of scattering hyperbolae. The amplitude of the reflected signal is proportional to the EM contrast between the two layers. On the site, it is either the sedimentary filling that can cause this reflectivity, or the presence of buried objects, marked by a break in the lateral continuity of the filling, or the presence of localized diffractions (*e.g.* Yannah *et al.*, 2019).

Measurements were acquired with a Malå PROex (Guideline Geo AB, Sweden). Three north-south and 4 west-east profiles were acquired using 250 MHz shielded antennas with the source-receiver offset of 0.36 m. Results being redundant, only one N-S and one W-E profile will be further presented (gpr01, 145 m-long, and gpr02, 45 m-long, in Fig. 3, respectively). Antennas were moved along profiles to get images of the amplitude of the reflected EM wave as a function of the two-way travel time. One trace was acquired each 0.1 m using an encoder measuring wheel. Geolocalization was conducted each 5 m (profile gpr01) and 1.5 m (profile gpr02) along the profiles with an RTK differential GNSS. To obtain a more precise topography, a topographic cross-section along each GPR profile was extracted each 1 m from the LiDAR DEM, interpolated each 0.1 m, and finally associated with each GPR trace.

The knowledge of the EM propagation velocity is required to transform the two-way-traveltime sections into distance-depth images. This was achieved with 1 common mid-point survey (CMP; cmp01 in Fig. 3). For that, two unshielded, 200 MHz antennas were moved away from a central reference point with an increment of 0.2 m. The analysis of the reflection hyperbolae allowed for determining the distribution of EM wave velocity according to time through a semblance analysis. A constant velocity of 10.3 cm/ns was

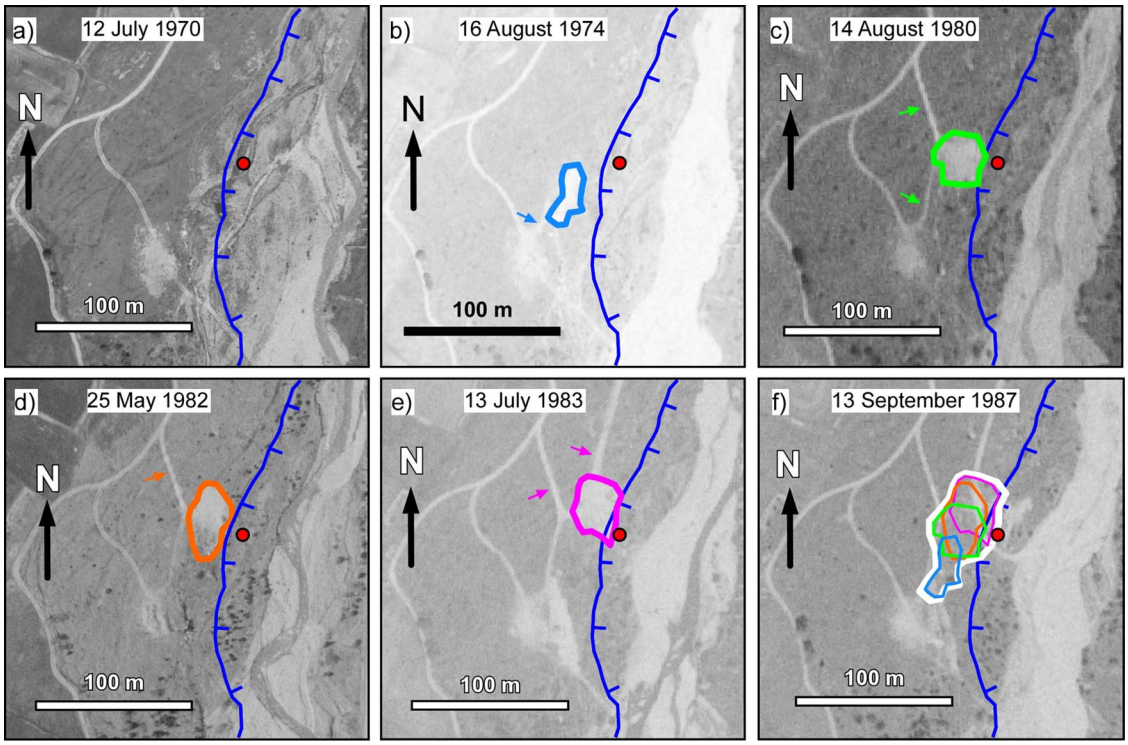

Figure 4 Analysis of historical aerial photographs publicly available from the French Geographic Institute (IGN; remonterletemps.ign.fr). On each photograph are shown the location of the river western bank in March 2021 (blue line), the perimeters of the identified successive platforms (coloured polygons), access tracks (coloured arrows) and the landfill uncovered in September 2020 (red dot). **a)** 12 July 1970; **b)** 16 August 1974; **c)** 14 August 1980; **d)** 25 May 1982; **e)** 13 July 1983; **f)** 13 September 1987, with the white polygon representing the total extent of the platform.

then chosen. All GPR data were processed using the Seismic Un*x Package (Stockwell, 1999) using a classical chain gathering: a [60–500 MHz] band-pass filter, trace by trace normalization, time gain amplification, topographic corrections and time to depth conversion using the constant velocity deduced from CMP data.

Geotechnical Prospecting

Ten excavations (p1 to p10; location in Fig. 3) were conducted in October 2022. They were located using the interpretation of remote sensing and geophysical results. They were conducted with mechanical excavators to maximum depths of 3 m. Wastes were manually sorted and individual logs were built. Results will be briefly synthesized in section 4 and more detailed in section 5, in relationship with the geophysical interpretation.

RESULTS

Analysis of Historical Aerial Photographs

Sixteen aerial photographs from 1948 to 2020 were visually analysed. Nothing is evidenced up to 1970 (Fig. 4a). Six pictures showing surface changes from July 1970 to September 1987 are presented in Fig. 4. Starting from August 1974 and up to July 1983 (Figs. 4b to 4e), pictures evidence the removal of vegetation (patches a few tens of m wide with a whitish colour suggesting bare ground) with various extents and a progressive northward displacement as a function of time. Tracks granting access to these zones also appear as the zones change (arrows in the figures). These are interpreted as the setting of technical platforms for landfilling. Once the surface had been entirely occupied by MSW pits, it was abandoned and the filling moved northward as suggested by the progressive creation of further platforms. In September 1987 (Fig. 4f), all of the surfaces are covered by vegetation. This suggests that the use of this area for landfill (during around 15–20 yr according to the temporal resolution provided by the aerial photographs) was already abandoned at this time. The total extent of the platform is shown as a white polygon in Fig. 4f with a corresponding surface of 1,930 m^2. Finally, these observations highlight that between the end of landfilling (around 1987) and the geotechnical design of earthworks (around 2015), the historical knowledge of the exact location of the MSW landfill was forgotten.

Surface Morphology

Figure 5a presents the surface morphology of 2012 retrieved from the LiDAR DEM and its interpretation is shown in Fig. 5b. The map shows a southward-decreasing elevation with an average value of 1,086 m above sea level (asl) over the study site. Several lineaments, with

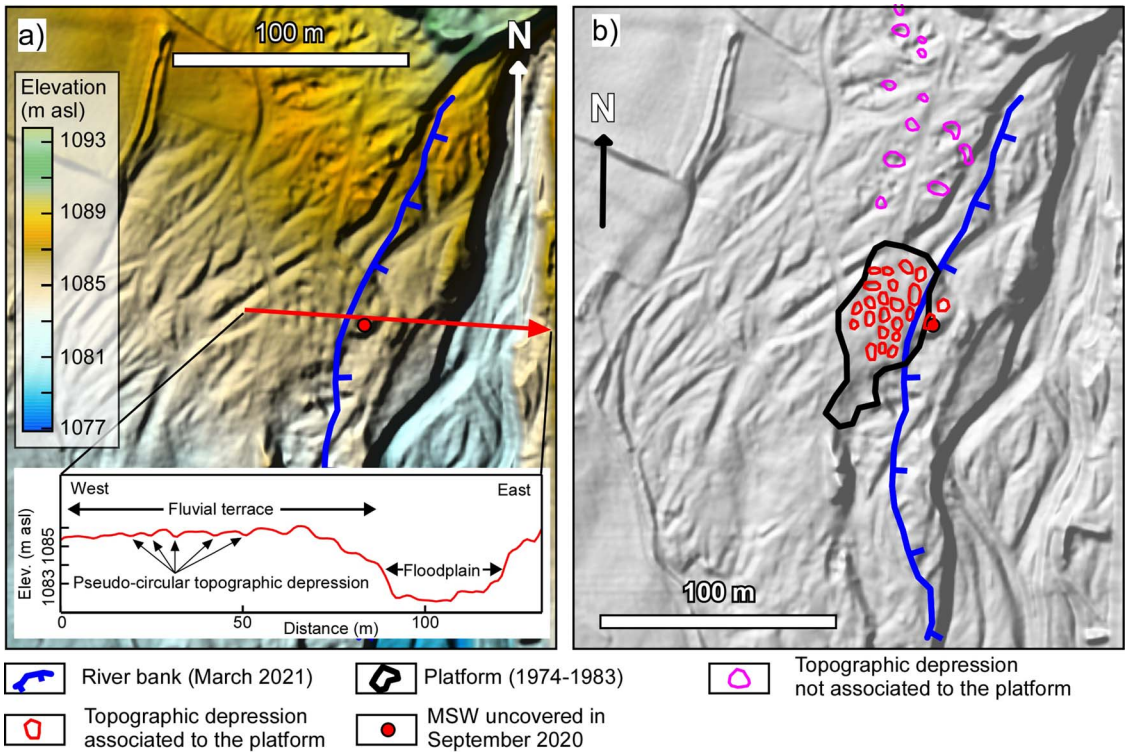

Figure 5 Surface morphology from LiDAR DEM (2012). **a)** DEM. The red line corresponds to the location of the topographic cross-section at the bottom of the map. **b)** Hillshade with mapping of pseudo-circular depressions. The extent of the platform interpreted from aerial photographs in Figure 4f is shown as well as the location of the MSW uncovered in September 2020 (red filled dot).

orientations varying between north/south and northeast/southwest, correspond to the river bed, the floodplain and, to the west, former alluvial terraces. In the central part of the map, several pseudo-circular topographic depressions are visible. They exhibit average widths of several metres at most with corresponding surfaces ranging between ~7 and 35 m^2. The depth of these depressions ranges between 0.1 and 0.4 m (see topographic cross-section in Fig. 5a), which makes some of them difficult to identify in the field.

A large majority of these depressions (red polygons in Fig. 5b) are close to each other and are embedded in the area previously interpreted as the platform used for landfilling (Fig. 4). These depressions could originate from differential compaction between, on the one hand, the natural horizons made of coarse sediments poorly prone to compaction and, on the other hand, pits filled with compactible materials such as plastic and soil. Suffusion with the washing away of fine grains (as identified in the pits; Fig. 1c) could also lead to subsidence. Some other pseudo-circular depressions are observed to the north (green polygons in Fig. 5b) but they do not appear to be concentrated in a specific area.

Geophysical Investigations

Magnetic and electromagnetic mapping. The results of magnetic and electromagnetic mapping are presented in Fig. 6. Magnetic mapping was conducted over a surface of around 42,000 m^2. After filtering, around 42,950 experimental measurements were retained, providing an average density of around 1 pt/m^2 (around 12 pt/m^2 inside and in the vicinity of the platform and looser away). Results for the vertical gradient of the magnetic field are shown in Fig. 6a. To highlight the most probable anomalies, a homogeneous zone with values around 0 was selected (1.3×10^{-2} km^2; around 5,000 experimental data). Average ($\mu = 0$ nT/m) and standard deviation ($\sigma = 7$ nT/m) were computed to keep data within the 99% confidence interval by discarding data within the $\mu \pm 3\ \sigma$ range (i.e. from −21 to 21 nT/m). The strongest anomaly is located over the platform identified from aerial photographs. It is noticeable that the boundaries identified by aerial photographs and magnetic mapping match remarkably well. Two punctual anomalies are also visible to the south, outside the platform (red polygons in Fig. 6a). Finally, small topographic depressions are identified north of the platform (purple polygons in Fig. 6a). They do not exhibit any magnetic anomaly.

Electromagnetic induction mapping. EMI-HCP mapping was conducted over a surface of 24,470 m^2 (Fig. 6b). Raw data revealed strong negative and positive values over the platform that are attributed to the presence of metallic elements at depth and at the surface. After filtering the noisy data (ρ_a lower than 10 Ωm and higher than 6,000 Ωm), around 20,700 experimental points were kept. This led to an average measurement

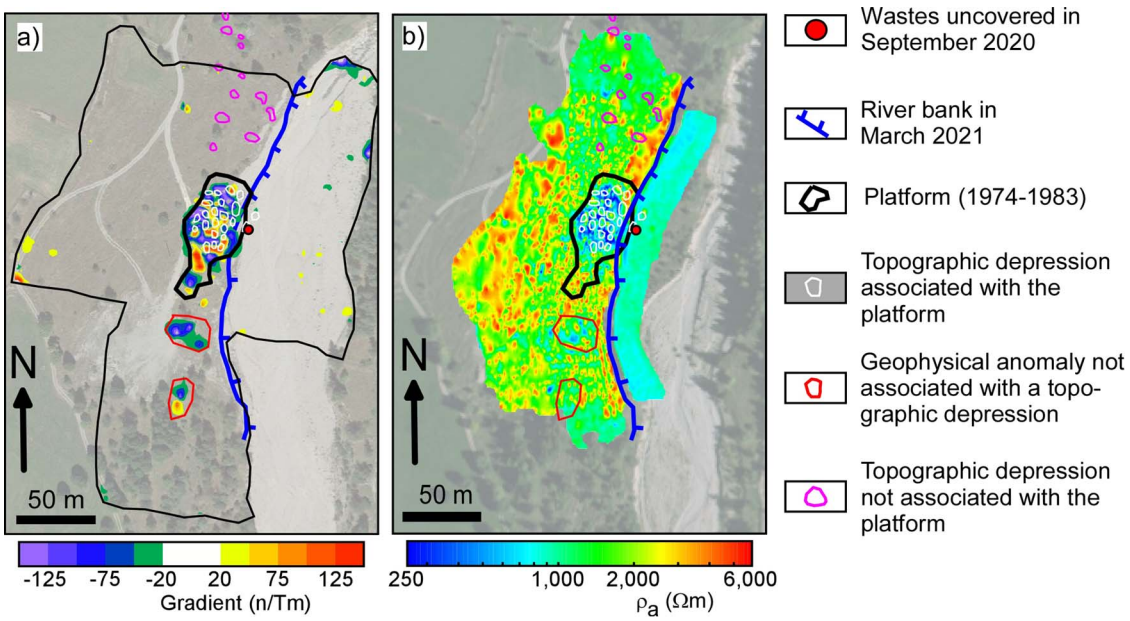

Figure 6 Magnetic and electromagnetic mapping. **a)** Map of the vertical gradient of the magnetic field with values lower than $\pm 3\sigma$ blanked. **b)** Electromagnetic induction mapping in Horizontal Co-Planar coil orientation mode. The data extend from 25 to 6,000 Ωm. For the sake of clarity, the colorscale has been reduced to a range 250-6,000 Ωm.

density of around 0.9 pt/m^2 (1.7 pt/m^2 inside and in the vicinity of the platform, and looser away). Experimental data were then interpolated using the same grid as for magnetic mapping. The resulting map shows apparent resistivity ranging between 25 and 6,000 Ωm. However, to better highlight low resistivity zones, the lower bound of the colorscale was limited to 250 Ωm.

Results show that apparent resistivity ranges mainly between 500 and 2,500 Ωm (87% of the experimental data). This range corresponds to fluvial sediments present below ground. This range is in agreement with the resistivity of coarse sediments made of sand to cobbles (*e.g.* Reynolds, 2011). In the river bed, however, apparent resistivity is slightly lower (between 700 and 1,000 Ωm) and could indicate a higher moisture content.

Then, the lowest apparent resistivity on the map is observed within the platform, with values in the range 25–50 Ωm. It is also noticeable that, within the platform, two pits located at its north-eastern boundary do not exhibit low resistivity but, on the contrary, resistivity greater than 1,500 Ωm (Fig. 6b). This will be discussed further.

Seismics. Figure 7 presents the P-wave tomogram with the results of the traveltime analysis for the two end-shots superimposed. The image shows an upper layer with a P-wave velocity (*Vp*) of 400 m/s overlying an horizon with *Vp* ranging between 1,900 and 2,500 m/s. The interface between these two units is horizontal and located at a depth of 10 m.

Electrical resistivity. The locations of the two ERT profiles are shown in Fig. 3 and the results are presented in Fig. 8. The first 32 m along profile ert01 (Fig. 8a) is located outside the platform and shows the resistivity distribution of the undisturbed subsurface. From top to base, it shows high resistivity ($\rho > 4{,}000$ Ωm) over the first ≈ 5 m, intermediate resistivity (≈2,000–2,500 Ωm) over a thickness varying laterally between 0.5 and approximately 8 m and, finally, resistivity lower than 1,500 Ωm at depth. Inside the perimeter of the platform and within the first horizon, lateral discontinuities are

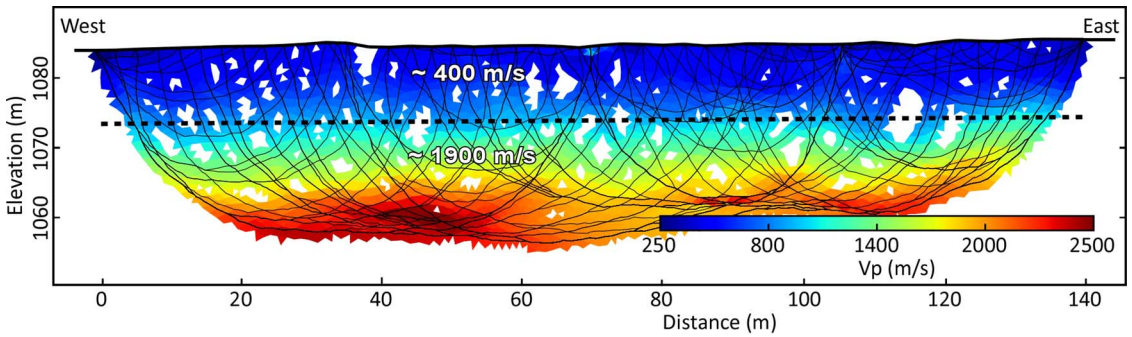

Figure 7 P-wave velocity analysis along profile sp01 (location in Fig. 3). The results of the refraction analysis for the two end-shots is superimposed on the tomogram (P-wave velocity in the horizons and location of the interface as a black dashed line).

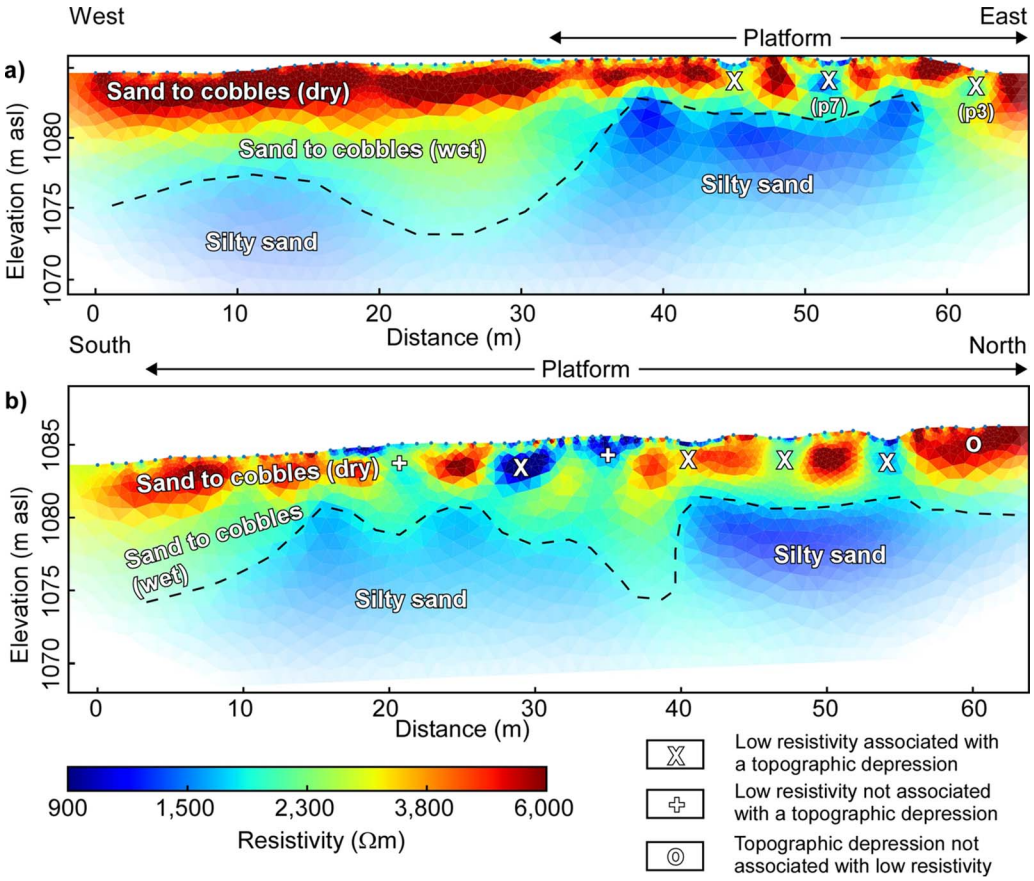

Figure 8 Electrical resistivity tomography (location of the profiles in Fig. 3). **a)** Profile ert01. p3 and p7 refer to excavations. **b)** Profile ert02.

observed in the form of low resistivity zones (down to 575 Ωm), with widths of a few metres and depths limited to around 3 m.

Ground-Penetrating radar. The analysis of the CMP sounding (cmp01 in Fig. 3 for location) provided an EM wave velocity ranging between 9.5 and 10.5 cm/ns (Figs. 9a and 9b). An average of 10.3 cm/ns was used for time-depth conversion. Also, from the EM wave velocity, it is possible to derive the dielectric permittivity K which is partially controlled by the volumetric water content θ (Huisman *et al.*, 2003). A value of 9 was found considering a velocity of 10 cm/ns. It was further used to evaluate the volumetric water content in the first metres below the ground surface using the empirical relationship proposed by Topp *et al.* (1980) and a value of around 17% was found for these measurements (conducted in March 2021 with snow cover).

The location of GPR sections gpr01 and gpr02 is shown in Fig. 3 and the results are presented in Figs. 9b and 9c, respectively. Images show strong attenuation starting from approximately 3 m depth. Some lateral continuity between the sedimentary layers is observed in places but it is generally poor. Figure 9d presents a subset profile gpr02, where discontinuous areas can be observed and where attenuation seems to be more important starting from around 1 m depth. This is highlighted by purple ellipses in Fig. 9d.

Geotechnical Prospecting

The synthesis of geotechnical prospecting is presented in Fig. 10. Their location is provided in Fig. 10a and a synthetic log in Fig. 10b. All logs indicate the presence of a sedimentary cover (made of sand, gravels and cobbles), the average thickness and standard deviation of which is 0.5 and 0.3 m, respectively. they contain a low amount of waste, which is less than 5% in average. The average depth of the waste pits is 2.6 m with a moderate variability (σ = 0.3 m). The waste content ranges between 40 and 80% (average of 65%), and half of the waste elements are smaller than 0.5 m in size. The analysis of their nature revealed a high variability: plastic, glass, wood, ashes, pills, concrete, bricks and metallic elements. Big wastes were also found, among which a car engine, a motorcycle and an oven. Of particular interest are the contents of p3 and p7 (location in Fig. 10a) which are located right below the ERT profile. They have a similar amount of waste (approximately 70%) but much more metallic elements were found in p7. Also, p10 showed to contain a few quantity of metallic elements and, among others, glass, polystyrene, wood, ashes and plastic bags. This will be discussed in section 5. Finally, the subsurface was excavated down to an average depth of 3 m (around 0.4 m below the base of the pits). The analysis

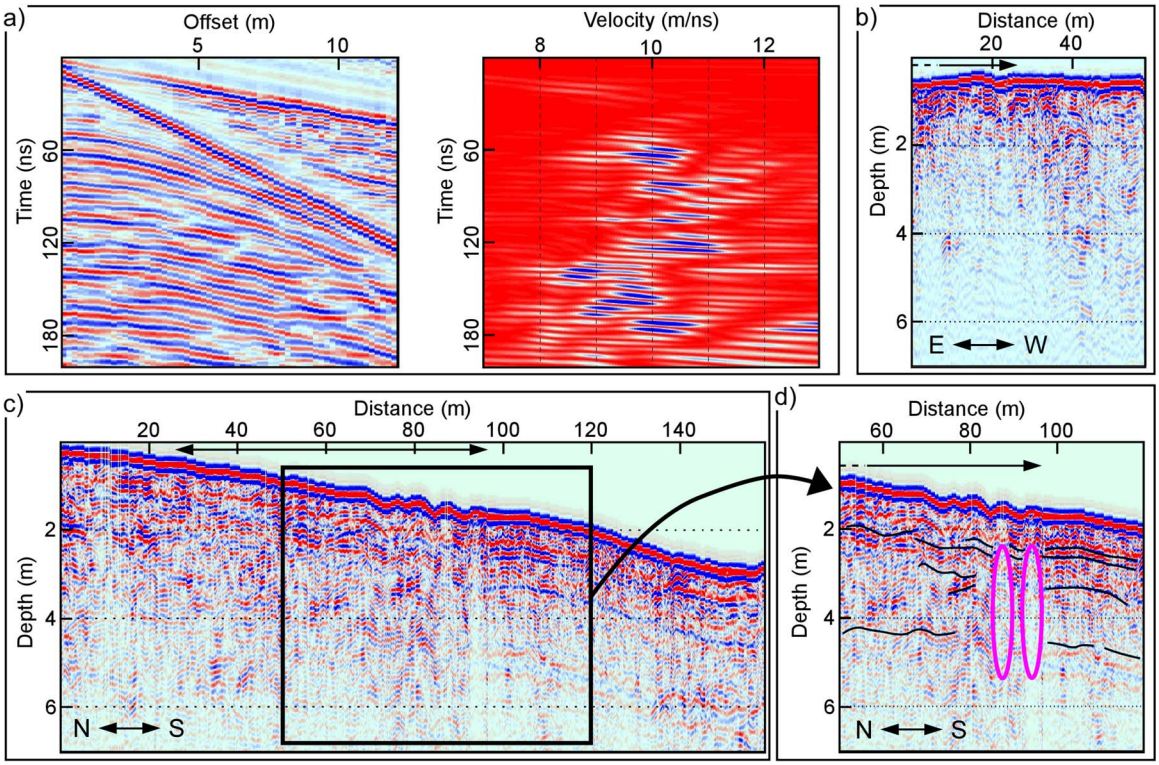

Figure 9 Ground-penetrating radar analysis (location in Fig. 3). **a)** cmp01 gather (left) and semblance velocity (right). **b)** Profile gpr02. **c)** Profile gpr01. **d)** Subset of the central part of profile gpr01. Black arrows at the top of profiles in Figs. 9b, 9c and 9d represent the extension of the platform.

of the samples showed the presence of alluvial sediments (from sand to cobbles) with a low amount of wastes (< 5%).

SYNTHESIS AND DISCUSSION

The analysis of historical aerial photographs suggests that platforms were established on the alluvial terrace of the western bank of the river. These contiguous platforms were used between 1974 and 1983 to bury wastes (Fig. 4) and encompass a total surface of 1 930 m^2 (Fig. 11a). The morphological analysis of the LiDAR DEM acquired in 2012 reveals the presence of several pseudo-circular topographic depressions, a few meters in width and 0.1 to 0.4 m in depth. Most of these depressions are embedded within the platform. Some other topographic depressions were identified north of the platform (purple polygons in Fig. 5) but were not related to any magnetic or electromagnetic anomaly (purple polygons in Fig. 6). Their origin remains unknown but they are not considered here as MSW pits containing, notably, metallic elements such as those shown in Fig. 2c.

Thanks to observations provided by excavations, geophysical measurements can be further interpreted. From magnetic and electromagnetic mapping, the strongest gradient and lowest apparent resistivity values,

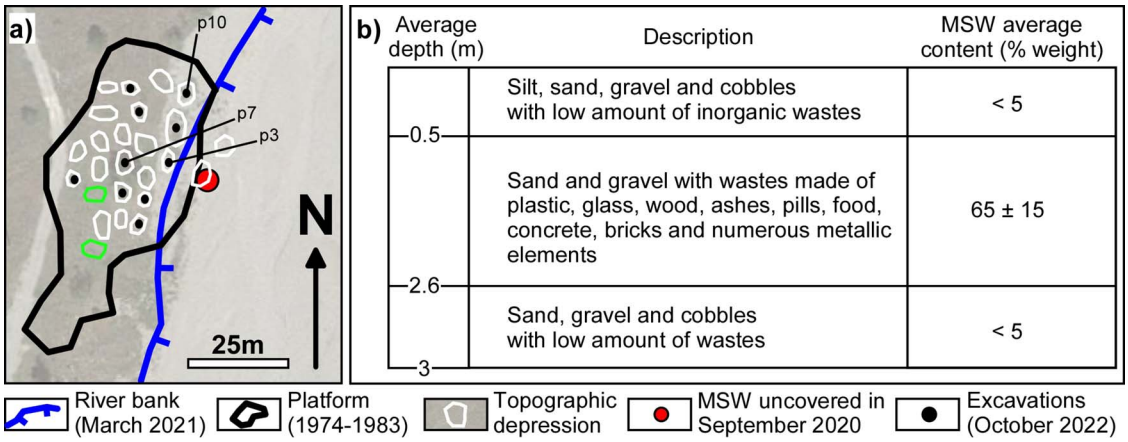

Figure 10 Geotechnical prospecting results. **a)** Location of 10 excavations among which p3, p7 and p10 are detailed in the text. **b)** Synthetic log.

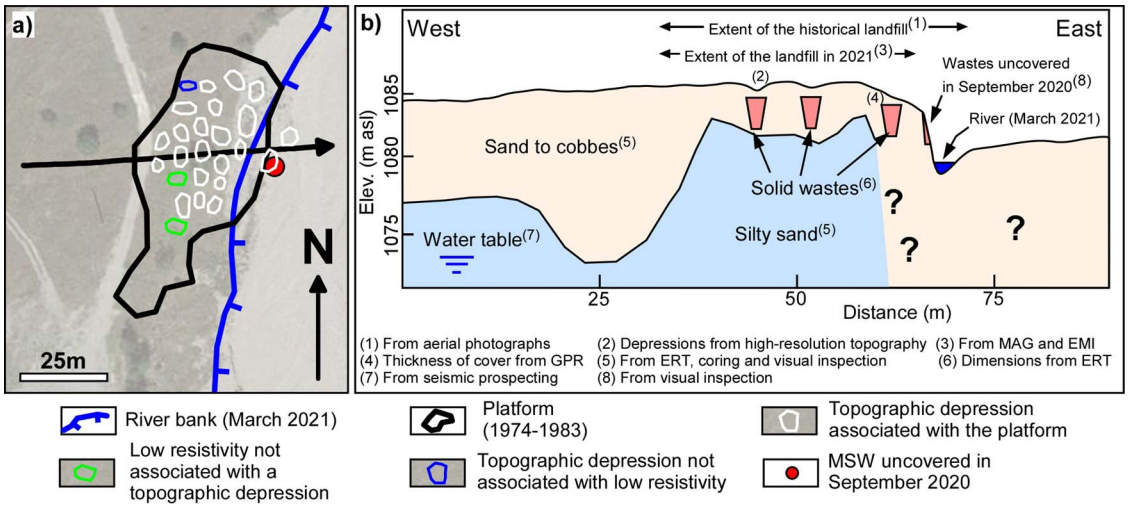

Figure 11 Geophysical and geotechnical synthesis. **a)** Location of the topographic and geophysical anomalies within the platform. The black arrowed line shows the location of the cross-section in Fig. 11c. **b)** Average geotechnical log following 10 excavations conducted to depths of around 3 m. **c)** Synthetic geotechnical cross-section (location in Fig. 11a).

respectively, are observed within the platform, in agreement with the presence of metallic elements (Fig. 6). In opposite, pit p10, located in the north-eastern part of the platform (location in Fig. 10a) contained a few amount of metallic elements compared to other excavated pits. In agreement, the MAG map shows no significant gradient above the pit, while the EMI map displays apparent resistivity values greater than 1,500 Ωm. Two punctual anomalies are also visible to the south (red polygons in Fig. 6a) from MAG mapping. These anomalies are not associated with topographic depressions and exhibit resistivity values greater than 2,500 Ωm, comparable to those obtained in fluvial sediments. This suggests that they are probably not associated with pits filled with a significant amount of metallic elements. This was confirmed in June 2021 by a visual inspection conducted without snow cover and during which metallic objects were observed at the surface. Finally, the topographic depressions identified north of the platform (purple polygons in Figs. 6) do not exhibit any magnetic or resistivity anomaly. They are consequently most probably not associated with pits filled with solid wastes comparable to those observed within the platform, embedding notably metallic elements. Their nature and origin remain difficult to assess.

Seismic results mainly show a strong P-wave velocity gradient ranging from 400 to 1,900 m/s, under the form of a sub-horizontal interface located at 9 m depth. This interface is interpreted as the water table with unsaturated fluvial sediments above. This suggests that the water table is not in direct contact with the MSW pits.

ERT images show more variability than the seismic tomography. The first layer below ground with high resistivity (>4,000 Ωm) corresponds to dry coarse fluvial sediments. The discrepancy between EMI and ERT measurements, where resistivity retrieved from ERT is higher by a factor of 2 to 3, can be partially explained by the period of measurements. ERT was conducted in June 2021 during a hot and dry period while EMI was conducted in winter with a wetter subsurface. The intermediate zone with an average resistivity of around 2,000–2,500 Ωm could correspond to the same but wet fluvial sediments. Finally, the low resistivity horizon observed at depth could correspond to wet silty sand by analogy with observations on the coring at similar depths (see section 2). This horizon shows important lateral variations in elevation that could correspond to one or several erosion phases by the river during periods of flood. This interpretation can be conducted similarly on profile ert02 (Fig. 8b). Then, low resistivity zones are observed in the globally highly-resistive first layer below ground. First, these low resistivity values are not observed outside the platform and cannot correspond to dry, coarse fluvial sediments. Second, most of these anomalies match topographic depressions ("X" in Fig. 8). They can then be interpreted as corresponding to MSW pits embedding notably metallic elements and soil/earth materials with low resistivity. Furthermore, the lateral extension of these low-resistivity zones matches that of the topographic depressions. This matches the spatial dimensions of the pits according to historical knowledge. Finally, 2 of these depressions were excavated (p3 and p7 in Fig. 8a). The results indicate that p7 contained more metallic elements, which is in agreement with this pit showing a lower resistivity on the ERT image. Other low resistivity zones are observed, but which are not associated with topographic depressions ("+" in Fig. 8b). Their interpretation remains cautious, and since none of them was excavated, geotechnical prospecting is required to assess their nature. A small topographic depression 0.1 m in depth was observed at the end of profile ert02 ("o" in Fig. 8b). This depression

is, however, not associated with low resistivity. On the contrary, it shows resistivity comparable to dry fluvial sediments (> 4,000 Ωm). Finally, it should be mentioned that no high resistivity is observed above the pits, which should correspond to the 0.5 m thick fluvial sediments used as a cover (Fig. 10b). This probably originates from their reduced thickness and the spatial resolution attended from the experimental setup with a unit electrode spacing of 1 m.

The estimation of the water content from GPR (approximately 17%) suggests that the first metres below the surface are unsaturated. It is in agreement with the location of the water table at 10 m depth from seismic prospecting. GPR profiles show that within the platform strong attenuation is observed in places starting from about 1 m depth. This can be interpreted as more conductive areas starting at these depths. The first metre below the ground surface could then correspond to coarse sediments that could have been used to cover the MSW in the pits. There is, however, a small discrepancy with excavation that revealed an average thickness of this cover of 0.5 m. In conclusion, even if the penetration depth appears adequate, the GPR signature of the pits in which objects were buried is not straightforward and remains questionable with this geophysical method. Similar results were previously reported (Green *et al.*, 1999; Yannah *et al.*, 2019; Kondracka *et al.*, 2021). In this context, GPR prospecting is probably not the most adapted method to detect these specific MSW pits. However, it provides an evaluation of the thickness of the surface cover over the pits (around 1 m in this study).

For the MSW pits, the topographic depressions most probably originate from the compaction the MSW landfill underwent since the pits were filled (between the mid-1970s and the mid-1980s; Fig. 4). The coarse sediments constituting the fluvial terrace have very low compressibility whereas MSW landfills have higher compressibility. Depending on the nature of the waste and on the stress applied, the compressibility of MSW is generally evaluated between 0.15 and 0.45 (Swati & Joseph, 2008; Gourc *et al.*, 2010; Chen *et al.*, 2012). Here, using an average height variation ΔH of 0.3 m and an initial height H of 2 m (base of the wastes at a depth of 3 m after ERT and 1 m of sediments as a cover after GPR) provides a ratio $\Delta H/H = 0.15$. This order of magnitude is in agreement with the nature of the MSW on the study site (ratio MSW/soil $\approx$ 2). Some other factors, such as suffusion, may also have washed fine-grained sediments out of the pits and contributed to subsidence. As such, high-resolution topographic mapping using the LiDAR technique proves to be successful at detecting low amplitude topographic variations on the order of a few tens of cm. These LiDAR measurements are classically acquired from planes or helicopters and remain expansive, especially for small municipalities. However, LiDAR acquisition from Unmanned Aerial Vehicles (UAV) is increasingly used and could provide affordable ways to prospect areas with limited spatial extents (Gasperini *et al.*, 2014). Moreover, flights using drones are generally conducted a few tens of m high and can provide ground resolution much higher (several cm to some tens of cm) than with a plane or helicopter (typically of the order of 1 to a few m). Finally, optical images acquired from UAV can also be considered to build a DEM if the surface to be investigated is made of bare ground (i.e. no bush or trees).

ERT results suggest that pits are 3 m deep at most (Fig. 8). GPR results suggest that the interface between the cover made of fluvial sediments and the landfill is located at around 1 m depth (Fig. 9). Making simplifying hypotheses such as vertical walls for the pits and using only pits corresponding to white polygons in Fig. 11a leads to a first-order estimation of the total surface area and volume for the most probable historical pits of 350 m^2 and 700 m^3, respectively. An interpretative geotechnical cross-section synthesizing observations and their origin is presented in Fig. 11b. It is worth mentioning that sparse data about the water table suggest that, even during periods of high water table level (March 2021), it is located several m below the pits. As such it might be only very rarely in contact with them. However, rainfall and snow melt can infiltrate into the pits and further join the water table, allowing potential leachate circulation.

In agreement with Green *et al.* (1999), it is worth noting that no single geophysical parameter was capable of providing all the observations required for the location and volume estimation of the MSW pits. Mapping techniques allowed the precise delineation of the landfill's spatial extent with some limitations for EMI mapping due to poor spatial sampling on the eastern border of the platform. These results confirm previous studies (Green *et al.*, 1999; Clément *et al.*, 2011; Dumont *et al.*, 2017; Appiah *et al.*, 2018) and the efficiency of these techniques for fast investigation of MSW landfill. However, these techniques failed at locating individual pits. Also, GPR did not evidence individual pits unequivocally. Finally, ERT was successful at detecting pits and evaluating their width and depth but somewhat failed at imaging the sedimentary cover of each pit. Furthermore, considering the width of the pits (a few m) and the required spatial resolution to image them satisfactorily (electrode spacing of 1 m), a complete imaging of the landfill (area of around 50 m × 50 m) using 3D measurements appears unrealistic. Several tens of 2D profiles could be acquired and further inverted in 3D but it would cease to be cost-effective.

On the contrary, the methodology adopted in this work appears suitable and cost-effective. It takes advantage of the property of MSW pits to endure settlement and to be easily distinguished from the natural subsurface using high-resolution topography. First,

these topographic data can be acquired using UAVs equipped with LiDAR scanners or optical cameras. Second, fast ground mapping techniques (magnetics and/or electromagnetics) provide the precise extent of the fill. Third, quantitative imaging techniques (ERT) along selected profiles provide the evaluation of the spatial extent (width and depth) of the imaged pits. Fourth and in the case the cover over each pit is not imaged by ERT, GPR can provide an evaluation of its thickness.

CONCLUSION

A historical MSW landfill located in a mountainous valley in the French western Alps was investigated using remote sensing (aerial and satellite images, light detection and ranging digital elevation model) and ground geophysical techniques (magnetic and electromagnetic mapping, electrical resistivity tomography, ground-penetrating radar). The objective was to locate precisely a historical municipal solid waste landfill made of several pits a few metres in width, the exact location of which was forgotten. Following earthworks and two further floods that eroded into the river bank in 2020, one of the pits was uncovered. It showed the presence of plastic and metallic elements along with soil/earth. The analysis of historical aerial photographs through surface changes showed that the landfill started operating around 1974 and was sealed by 1987. It allowed the delineation of a platform of a surface of around 1930 m^2. The analysis of a high-resolution digital elevation model acquired in 2012 revealed the presence of numerous topographic depressions 0.1 to 0.4 m in depth and a few metres in width. Most of these depressions are located within the previously identified platform. Results of geophysical prospecting showed that almost all depressions located within the platform exhibit anomalies which can be associated with these depressions and the presence of wastes that underwent compaction. A rough estimation led to a total volume of wastes of around 700 m^3. Topographic depressions located outside the platform did not exhibit any geophysical anomaly and their nature remains unknown.

It is noticeable that no technique used alone allows the evaluation of both the extent and depth of the pits. On the contrary, the combination of mapping and imaging techniques provides fair results to evaluate a first-order quantity of the buried MSW. The combination of remote sensing and ground geophysical techniques showed to be efficient to locate the municipal solid waste landfill. The methodology employed in this study is applicable to detect any landfill exhibiting compaction.

Declaration of Competing Interest

The authors declare that they have no known competing financial interests or personal relationships that could have appeared to influence the work reported in this paper.

References

Appiah, I., Dotse Wemegah, D., Sarpong Asare, W. D., Danuor, S. K., and Forson, E. D., 2018, Integrated geophysical characterisation of Sunyani municipal solid waste disposal site using magnetic gradiometry, magnetic susceptibility survey and electrical resistivity tomography: Journal of Applied Geophysics, **153**, 143-153.

Baek, W. K., Jung, H. S., Jo, M. J., Lee, W. J., and Zhang, L., 2019, Ground subsidence observation of solid waste landfill park using multi-temporal radar interferometry: International Journal of Urban Sciences, **23**, 406-421.

Biotto, G., Silvestri, S., Gobbo, L., Furlan, E., Valenti, S., and Rosselli, R., 2009, GIS, multi-criteria and multi-factor spatial analysis for the probability assessment of the existence of illegal landfills: International Journal of Geographical Information Science, **23**, 1233-1244.

Chen, K. S., Chen, R. H., and Liu, C. N., 2012, Modeling municipal solid waste landfill settlement: Environmental Earth Sciences, **66**, 2301-2309.

Clément, R., Legchenko, A., Quetu, M., Descloîtres, M., Oxarango, L., Guyard, H., and Girard, J., 2011, Experimental study of domestic waste material using magnetic resonance measurements: Near Surface Geophysics, **9**, 179-185.

Dahlin, T., and Zhou, B., 2006, Multiple-gradient array measurements for multichannel 2D resistivity imaging: Near Surface Geophysics, **4**, 113-123.

De Wet, A., 2016, Discovering and characterizing abandoned waste disposal sites using LiDAR and aerial photography: Environmental and Engineering Geoscience, **22**, 113-130.

Demanet, D., 2000, Tomographies 2D et 3D à partir de mesures géophysiques en surface et en forage: PhD Thesis, Université de Liège, Belgium.

Di Fiore, V., Cavuoto, G., Punzo, M., Tarallo, D., Casazza, M., Guarriello, S. M., and Lega, M., 2017, Integrated hierarchical geo-environmental survey strategy applied to the detection and investigation of an illegal landfill: A case study in the Campania Region (Southern Italy): Forensic Science International, **279**, 96-105.

Di Maio, R., Fais, R., Ligas, P., Piegari, E., Raga, R., and Cossu, R., 2018, 3D geophysical imaging for site-specific characterization plan of an old landfill: Waste Management, **76**, 629-642.

Dumont, G., Robert, T., Marck, N., and Nguyen, F., 2017, Assessment of multiple geophysical techniques for the characterization of municipal waste deposit sites: Journal of Applied Geophysics, **145**, 74-83.

Friedel, S., 2003, Resolution, stability and efficiency of resistivity tomography estimated from a generalized inverse approach: Geophysical Journal International, **153**, 305-316.

Gasperini, D., Allemand, P., Delacourt, C., and Grandjean, P., 2014, Potential and limitation of UAV for monitoring subsidence in municipal landfills: International Journal of Environmental Technology and Management, **17**, 1-13.

Gourc, J. P., Staub, M. J., and Conte, M., 2010, Decoupling MSW settlement into mechanical and biochemical processes – Modelling and validation on large-scale setups: Waste Management, **30**, 1556-1568.

Green, A., Lanz, E., Maurer, H., and Boerner, D., 1999, A template for geophysical investigations of small landfills: The Leading Edge, **18**, 248-254.

Günther, T., Rücker, C., and Spitzer, K., 2006, Three-dimensional modelling and inversion of DC resistivity data incorporating topography - II. Inversion: Geophysical Journal International, **166**, 506-517.

Huisman, J. A., Hubbard, S. S., Redman, J. D., and Annan, A. P., 2003, Measuring soil water content with ground penetrating radar: a review: Vadose Zone Journal, **2**, 476-491.

Keary, P., Brooks, M., and Hill, I., 2002, An introduction to geophysical exploration: Blackwell Publishing, Oxford, England.

Kondracka, M., Stan-Kłeczek, I., Sitek, S., and Ignatiuk, D., 2021, Evaluation of geophysical methods for characterizing industrial and municipal waste dumps: Waste Management, **125**, 27-39.

Martínez-Segura, M. A., Vásconez-Maza, M. D., and García-Nieto, M. C., 2020, Volumetric characterisation of waste deposits generated during the production of fertiliser derived from phosphoric rock by using LiDAR and electrical resistivity tomography: Science of The Total Environment, **716**, 137076.

McNeill, J. D., 1980, Electrical terrain conductivity measurement at low induction numbers: Technical Report, Geonics Ltd, Mississauga, Canada.

Osinowo, O. O., Falufosi, M. O., and Omiyale, E. O., 2018, Integrated electromagnetic (EM) and electrical resistivity tomography (ERT) geophysical studies of environmental impact of Awotan dumpsite in Ibadan, southwestern Nigeria: Journal of African Earth Sciences, **140**, 42-51.

Reynolds, J. M., 2011, An introduction to applied and environmental geophysics: Wiley-Blackwell, Chichester, England.

Rücker, C., Günther, T., and Spitzer, K., 2006, Three-dimensional modelling and inversion of DC resistivity data incorporating topography - I. Modelling: Geophysical Journal International, **166**, 495-505.

Rücker, C., Günther, T., and Wagner, F. M., 2017, pyGIMLi: An open-source library for modelling and inversion in geophysics: Computers & Geosciences, **109**, 106-123.

Silvestri, S., and Omri, M., 2008, A method for the remote sensing identification of uncontrolled landfills: formulation and validation: International Journal of Remote Sensing, **29**, 975-989.

Soupios, P., and Ntarlagiannis, D., 2017, Characterization and monitoring of solid waste disposal sites using geophysical methods: current applications and novel trends. In: Sengupta, D. & Agrahari, S. (Eds.): Modelling trends in solid and hazardous waste management, Springer.

Soupios, P., Papadopoulos, N., Papadopoulos, I., Kouli, M., Vallianatos, F., Sarris, A., and Manios, T., 2007, Application of integrated methods in mapping waste disposal areas: Environmental Geology, **53**, 661-675.

Stockwell, J. W. Jr., 1999, The CWP/SU: Seismic Un*x package: Computers & Geosciences, **25**, 415-419.

Swati, M., and Joseph, K., 2008, Settlement analysis of fresh and partially stabilised municipal solid waste in simulated controlled dumps and bioreactor landfills: Waste Management, **28**, 1355-1363.

Topp, G. C., Davis, J. L., and Annan, A. P., 1980, Electromagnetic determination of soil water content. Measurements in coaxial transmission lines: Water Resources Research, **16**, 574-582.

Yannah, M., Martens, K., Van Camp, M., and Walraevens, K., 2019, Geophysical exploration of an old dumpsite in the perspective of enhanced landfill mining in Kermt area, Belgium: Bulletin of Engineering Geology and the Environment, **78**, 55-67.

Acknowledgments

The authors thank the project manager, namely the Syndicat Mixte des Bassins Hydrauliques de l'Isère (SYMBHI, Grenoble, France), for providing the LiDAR DEM and geophysical data, and allowing to publish them. The authors are part of Labex OSUG@2020 (Investissements d'avenir - ANR10 LABX56). The authors thank Claire Bouligand (ISTerre) for her help with the processing of magnetic data. This research did not receive any specific grant from funding agencies in the public, commercial, or not-for-profit sectors.

Data Availability Statement

Geophysical and LiDAR data presented here are not publicly available. Historical aerial photographs are publicly available from the French National Geographic Institute (IGN; remonterletemps.ign.fr). The Landsat/Copernicus satellite optical image from 05 September 2020 was retrieved from The Google Satellite repository. Geological maps and boreholes data are publicly available from the French Geological Survey (BRGM; infoterre.brgm.fr). However, for confidentiality reasons, the exact location of the study site is not provided.

Credit Author Statement

All authors contributed to all parts of the manuscript.